



Calving event size measurements and statistics of Equip Sermia, Greenland, from terrestrial radar interferometry

Andrea Walter^{1,2}, Martin P. Lüthi¹, Andreas Vieli¹

¹Institute of Geography, University of Zurich, Zurich, Switzerland

5 ²Laboratory of Hydraulics, Hydrology and Glaciology, ETH Zurich, Zurich, Switzerland

Correspondence to: Andrea Walter (andrea.walter@geo.uzh.ch)



Abstract. Calving is a crucial process for the recently observed dynamic mass loss changes of the Greenland ice sheet. Despite its importance for global sea level change, major limitations in understanding the calving process remain. This study presents calving event data and statistics recorded with a terrestrial radar interferometer at the front of Eqip Sermia, a marine terminating outlet glacier in Greenland. The data with a spatial resolution of several meters recorded at one-minute intervals was processed to provide source areas and volumes of 1700 individual calving events during a 6 day period. The calving front can be divided into sectors ending in shallow and deep water with different calving statistics and style. For the shallow sector, characterised by an inclined and very high front, calving events are more frequent and larger than for the vertical ice cliff of the deep sector. We suggest that the calving volume missing in our observations of the deep sector is removed by oceanic melt and subaquatic calving, which implies that subaqueous mass loss must be substantial for this sector with a contribution of up to 75 % to the frontal mass loss. The size distribution of the deep sector follows a power law, while the shallow sector is likely represented by a log-normal model. Variations in calving activity and style within the sectors seem to be controlled by the bed topography and the front geometry. Within the short observation period no clear relationship between environmental forcings and calving frequency or event volume could be detected.

1 Introduction

Over the past decade rapid retreat, thinning and flow acceleration of many outlet glaciers contributed substantially to the observed increasing mass loss of the Greenland ice sheet (Moon et al., 2012; Enderlin et al., 2014; King et al., 2018) and consequently to global sea level rise (Rignot et al., 2011; IPCC, 2014). These dynamic changes seem to be related to a general warming trend of air temperature and water masses in Greenland (Straneo et al., 2013). Several studies have shown a high sensitivity of outlet glaciers to environmental forcings (Holland et al., 2008; Howat et al., 2010; Carr et al., 2017), while the fjord topography is an important control for the dynamic behaviour of the outlet glaciers (Warren, 1991; Catania et al., 2018). However, major limitations in understanding and predicting the dynamics of outlet glaciers remain and the detailed relationship between climate and dynamic changes is still poorly understood (McFadden et al., 2011; Vieli and Nick, 2011; Straneo et al., 2013).

Calving is a crucial process controlling how tidewater glaciers react to changes in environmental conditions (Joughin et al. 2004; Thomas, 2004; Nick et al., 2009). Calving rates are controlled by the stress state at the terminus. When stresses exceed the strength of the ice, fractures can form and propagate and a block of ice can break off from the front. Mechanisms causing fractures to propagate are: 1) spatial gradients in the glacier velocity, 2) changes in frontal geometry (front position, height), 3) undercutting of the glacier front by melting at or below the water line and 4) buoyancy forces (Pralong and Funk, 2005; Benn et al., 2007). Direct and continuous observations of the calving process are difficult and therefore the underlying mechanisms are observationally under-constrained. Most existing studies investigated the calving process on longer time scales by considering time averaged calving rates or fluxes. Available studies on individual calving events focus mostly on discontinuous (Warren et al., 1995; O'Neel et al., 2003) or indirect measurements (O'Neel et al., 2010; Walter et al., 2010;



Bartholomäus et al., 2012; Glowacki et al., 2015). Several studies investigating the process of ice break-off over short time scales show that the process of calving has a very high temporal and spatial variability and that the observed calving size distribution for grounded tidewater glaciers is following a power law (Chapuis and Tetzlaff, 2014; Åström et al., 2014; Pęćlicki and Kinnard, 2016). However, these investigations focus mostly on time averaged estimates of volumes, discontinuous
5 datasets, indirect measurements or a combination thereof and thus lack continuous direct observations of the calving event size. For an accurate representation of the calving process in current flow models and to link calving activity with potential environmental forcings more detailed observations with high temporal and spatial resolution are necessary.

During the last 20 years observational data for monitoring calving glaciers was mainly obtained through satellites at a sampling frequency that is not suitable to observe individual calving events. Other more in-situ based approaches such as terrestrial
10 photogrammetry using time-lapse cameras (dependent on weather and daylight) (Vallot et al., 2019) and drone data (limited temporal resolution) (Jouvet et al., 2017) also show severe limitations regarding the observation of the highly variable calving process. Promising results were obtained with seismic monitoring of calving (Amundson et al., 2012; Walter et al., 2013; Bartholomäus et al., 2015) and maximum wave amplitudes as a proxy for calving fluxes (Minowa et al., 2018), but those methods can detect only large events and cannot quantify calving event volumes directly. Terrestrial laser scanning allows to
15 measure the volume of individual calving events (Pęćlicki and Kinnard, 2016), but requires suitable meteorological conditions and lacks the temporal resolution to detect individual calving events. Terrestrial radar interferometers can overcome most of the mentioned limitations and have been used to study the effects of tidal forcing on the front of an outlet glacier (Voytenko et al., 2015), to investigate calving rate and velocity (Rolstad and Norland, 2009), to determine calving event frequency (Chapuis et al., 2010), velocity variations and grounding line motion (Xie et al., 2018), glacier's response to calving (Cassotto
20 et al., 2018) or to estimate the volume of a single large calving event (Lüthi and Vieli, 2016).

This study aims at investigating the calving process and event statistics by using a terrestrial radar interferometer (TRI). For this purpose the calving front of the tidewater outlet glacier Eqip Sermia in Greenland was investigated with a TRI at one-minute intervals during a 6-day field campaign in 2016 and with a spatial resolution of several meters. The resulting high resolution time-series of individual calving event volumes and related source areas allow us to investigate the relationship
25 between calving front geometry, calving flux and environmental forcings such as tides or air temperature.

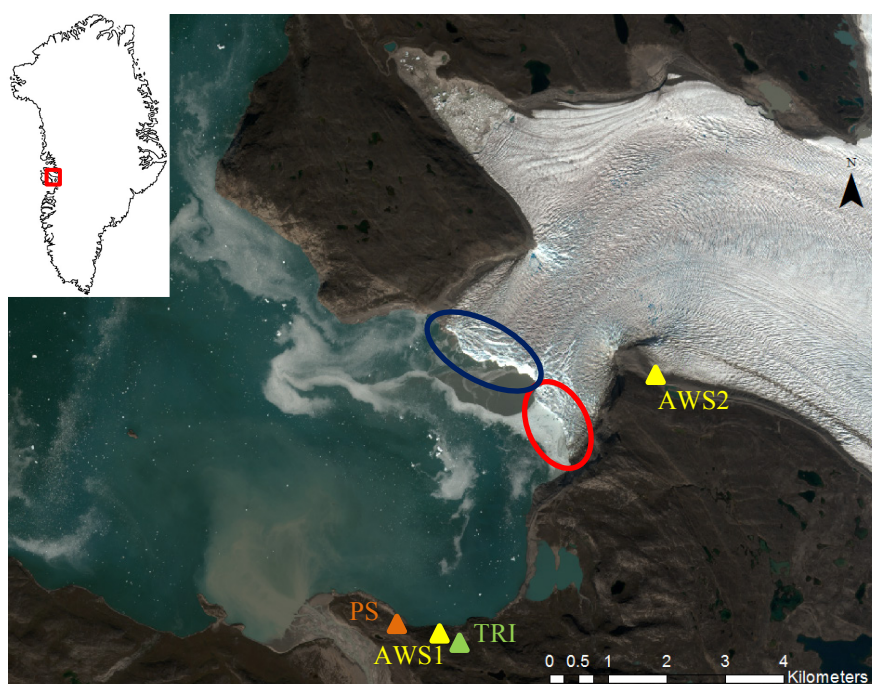
2 Study area and data acquisition methods

2.1 Study area

Eqip Sermia (69°47'N, 50°15'W) is an ocean terminating outlet glacier located at the western margin of the Greenland ice sheet. Observations of the glacier front position, surface elevation and flow speed are available at almost decadal resolution
30 since 1912 and show a doubling of discharge and accelerated retreat within the last two decades (Lüthi et al., 2016). Between 1912 and 2006 velocities between 2.5 and 5 m day⁻¹ were observed, whereas today the glacier front velocities are reaching up to 16 m day⁻¹.



The calving front has a width of 3.2 km and a height above the water line between 50 and 170 m. The whole front is grounded but the water depth in the northern half is very shallow (0 – 20 m, termed ‘shallow sector’ from now on) and locally the bedrock protrudes above the water. In the southern sector the water depth is 70 to 100 m (termed ‘deep sector’ from now on). Directly at the calving front no depth sounding data are available and the given depth estimates are extrapolated from bathymetric surveys in the proximity of the current front position (Rignot et al., 2015; Lüthi et al., 2016). Related to the contrast in water depth, the geometry of the front is also distinctly different between the two frontal sectors. In the deep southern sector the front is vertical and the frontal cliff height lower than in the shallow northern sector where the front is inclined (Fig. 1).



10 **Figure 1: Overview of Eqip Sermia and measurement sites. The positions of the terrestrial radar interferometer (TRI), the pressure sensor (PS) and the two weather stations (AWS) are indicated by triangles. The deep and shallow calving front sectors are marked with red and blue. Background: Sentinel-2A scene from 3 August 2016 (from ESA Copernicus Science Hub: <https://scihub.copernicus.eu>).**

15 2.2 Terrestrial radar interferometer

A terrestrial radar interferometer (TRI, Gamma GPR) was installed on bedrock 150 m above sea level across the bay of Eqip Sermia at 4.5 km distance (69.7523 N / 50.2520 W; Figs. 1, 2) with the line-of-sight in flow direction of the glacier. The measurements were repeated at one-minute intervals from 19 August 2016, 18:40 UTC to 27 August 2016, 10:30 UTC. This allowed us to produce an almost continuous record of velocity and elevation change over 7.65 days with a 1.53 days break (22 August 2016, 00:55 UTC to 23 August 2016, 13:00 UTC due to an instrument failure.



The Gamma GPRI is a real-aperture radar interferometer featuring one transmit and two receive antennas. Acquisitions are obtained by antenna rotation along the vertical on a precision astronomical mount. Consecutive interferograms from one of the receiving antennas are used to calculate the velocity. The two receiving antennas facilitate reconstruction of the topography. The radar interferometer operates at a wavelength of $\lambda = 17.4$ mm (Ku-Band, 17.2 GHz). The range resolution is approximately 0.75 m, while the azimuth resolution is 0.1 degrees corresponding to 7 m at a slant range of 4.5 km (Werner et al., 2008a).



Figure 2: The terrestrial radar interferometer (TRI) located opposite of the front of Equip Sermia at a distance of 4.5 km (image: M. P. Lüthi, 2016). The TRI has one transmit (TX) and two receive antennas (RX1, RX2).

10

2.3 Environmental data

Two automatic weather stations (AWS) with Decagon Em50 data loggers were installed at the sites indicated in Figure 1 and collected data in one hour intervals during the whole field campaign. AWS2 located next to the ice edge at 362 m a.s.l. (69.79442 N / 50.16115 W) measured air temperature and relative humidity (VP-3 Humidity Temperature and Vapor Pressure Sensor) and wind (DS-2 Sonic Anemometer). AWS1 near the TRI at 60 m a.s.l. (69.75556 N / 50.25301 W) measured additionally incoming shortwave radiation (PYR Solar Radiation Sensor) and precipitation (ECRN-100 High-Resolution Rain Gauge). The meteorological conditions at the ice edge (AWS2) are influenced by the ice sheet while at AWS1 next to the TRI it is more representative for the climate conditions at the shore of the fjord.

Tides and waves induced by calving were recorded in the fjord with a RBRsolo pressure sensor (PS; Fig. 1) at a sampling rate of two seconds. The pressure sensor was installed at the shore at a distance of 4.5 km from the ice front (69.75731 N / 50.26490

20



W, Fig.1). To protect the sensor from floating ice and moving rocks it was fixed in a metal pipe that was attached to a rock at the shore by a steel cable.

3 Data processing methods

3.1 TRI data processing

5 The GPRI transmits the radar signal from antenna TX and records it by the two receiver antennas RX1 and RX2, which enables spatial interferometry (Fig. 2). To reconstruct topography, interferograms were produced using a standard workflow following Caduff et al. (2015) using the Gamma software stack. The resulting interferograms were unwrapped, using stable features on bedrock as reference. Following Strozzi et al. (2012), the unwrapped phases were then converted to topography z :

$$z = \frac{\lambda}{2\pi} \frac{R}{B} \phi + \frac{B}{2} - \left(\frac{\lambda}{2\pi}\right)^2 \frac{\phi^2}{2B},$$

10 where $\lambda = 17.4$ mm is the wavelength, R the range to a point on the ground, $B = 0.25$ m the baseline between the two receiving antennas, and ϕ the measured interferometric phase. To reduce noise from atmospheric disturbances 10 elevation models were stacked. This noise is mainly due to phase shifts in the interferogram induced through changes in air pressure, temperature and humidity (Goldstein, 1995). The final elevation models have a resolution of 3.75 m in range and about 8 m in azimuth direction at the glacier front and were obtained at 10 min intervals over the whole campaign.

15 The accuracy of the so obtained DEMs was evaluated by comparison with a reference DEM on stable terrain. We chose the Arctic DEM (Porter et al., 2018) which on stable terrain outside the glacier yielded elevation differences around 5 m in flat areas and differences up to 10 m in steep areas. The variability between the calculated TRI elevation models on stable terrain was investigated by randomly choosing 30 values resulting in a mean variability of 1 m and a maximum variability of 5 m.

In a next step consecutive stacked elevation models were subtracted. The negative height changes at the glacier front were identified as calving events. The aerial extent of individual calving events were extracted with the watershed segmentation method from scikit-image (van der Walt et al., 2014) with a height change of 5 m as threshold. This threshold corresponds to the maximum variability of the height between elevation models on stable terrain outside the glacier. Height changes of less than 5 m are considered as noise and filtered out. Additionally, calving events smaller than 10 pixels and with a width smaller than 3 pixels were excluded as noise. When applying these filtering thresholds, the height changes on stable terrain are mostly removed. To exclude volume changes from collapsing seracs in the highly crevassed ice further upstream a mask around the glacier front was used. The mask is defined as a line along the front with a buffer of 20 pixels (approximately 75 m) on each side of the line. All height changes outside the mask were ignored in the data processing.

25 For visualization the radar image pixels were mapped into cartesian coordinates. Since resampling is a possible source of error, all calculations were performed in the radar geometry and only the final results were georeferenced. Nearest neighbour interpolation was used to resample the radar data to the cartesian UTM22N grid.



Next, we investigated whether the calving event sizes follow a size-frequency distribution. To test whether the measured calving volumes V are explained by an exponential ($e^{-\beta V}$), a log-normal ($\frac{1}{V} \exp[-\frac{(\ln V - \mu)^2}{2\sigma^2}]$) or a power-law ($V^{-\alpha}$) size frequency distribution a statistical analysis using the Python package powerlaw was applied (Alstott et al., 2014). The package uses maximum-likelihood methods (Clauset et al., 2009) and gives as result the log-likelihood ratio R , which is used to investigate which model fits the data better, and the probability value p , which tells if one can trust the sign of R and should be $p \geq 0.1$.

Ice flow velocities were calculated from consecutive interferograms of TRI acquisitions in one-minute intervals. To reduce noise, 120 interferograms were stacked before phase unwrapping with respect to a reflector on stable terrain. The unwrapped phases can then be converted into line-of-sight displacement $\delta = \frac{-\lambda\phi}{4\pi}$ (Werner et al., 2008b), with a displacement measurement sensitivity smaller than 1 mm.

3.2 Pressure sensor data processing

The pressure sensor (PS; Fig.1) recorded the water pressure in the fjord opposite of the calving front, which can then be converted to water height and thus the amplitudes of the tides and calving waves are known. A high-pass filter with a pass frequency of 0.001 Hz was used to extract the calving waves which were then compared with the calving events detected by the TRI. The tides were extracted with a low-pass filter and are compared with the extracted calving events in order to identify a potential relationship between the tides and the calving events.

4 Results

4.1 Flow velocities

Ice flow velocities from TRI data in vicinity of the calving front are presented in Figure 3a. Due to radar shadow, additionally Figure 3b has been created from a high resolution velocity field from repeated UAV surveys from August 2016 (Rohner et al. 2019). Speeds are increasing towards the calving front with highest values of 16 m day^{-1} . Along the front the velocities are non-uniform, with two areas of high velocities separated by a frontal area where a bedrock ridge was visible during the field campaign (orange bar in Fig. 3; inset of Fig. 4). Further upstream the glacier velocity field is more uniform with generally higher velocities in the centre.

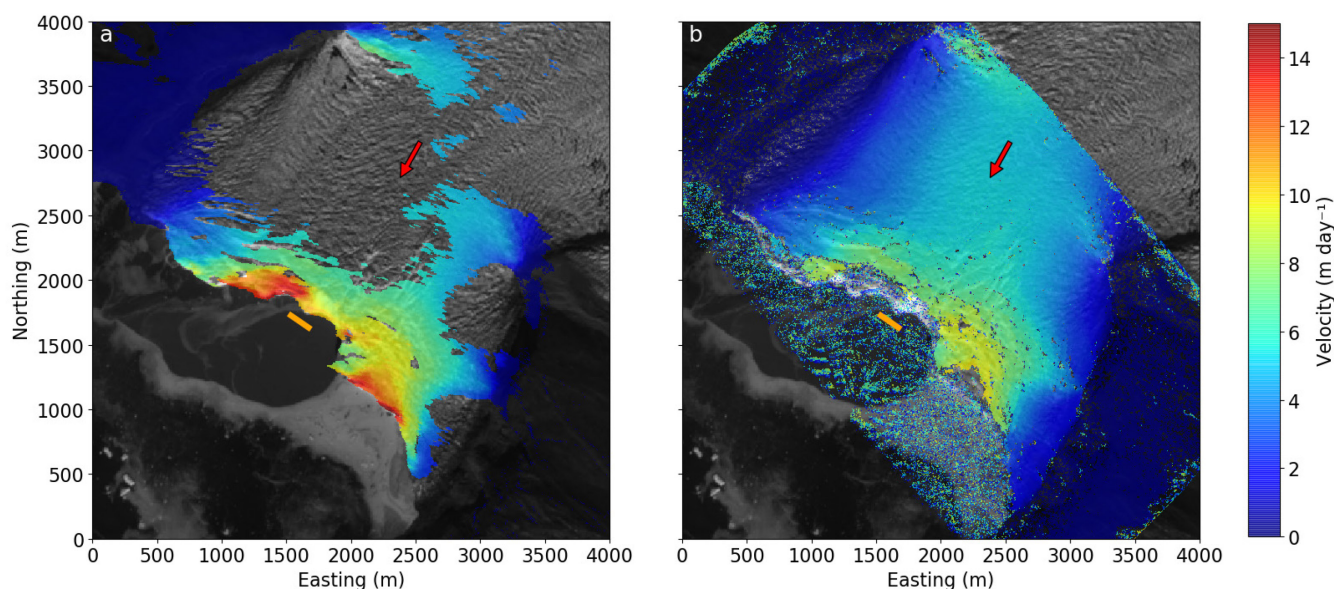
4.2 Magnitude and source area of calving events

During the field campaign 2016 a total of 1681 calving events were identified within 6.12 days with a mean event volume of 11700 m^3 . Due to the distinctly different characteristics in cliff geometry and water depth we analysed the two sectors along the front separately. Within the shallow sector 1403 events were found, while within the deep sector only 289 events were identified. This results in a mean calving activity of 9.5 events per hour in the shallow sector and 2.0 events per hour in the

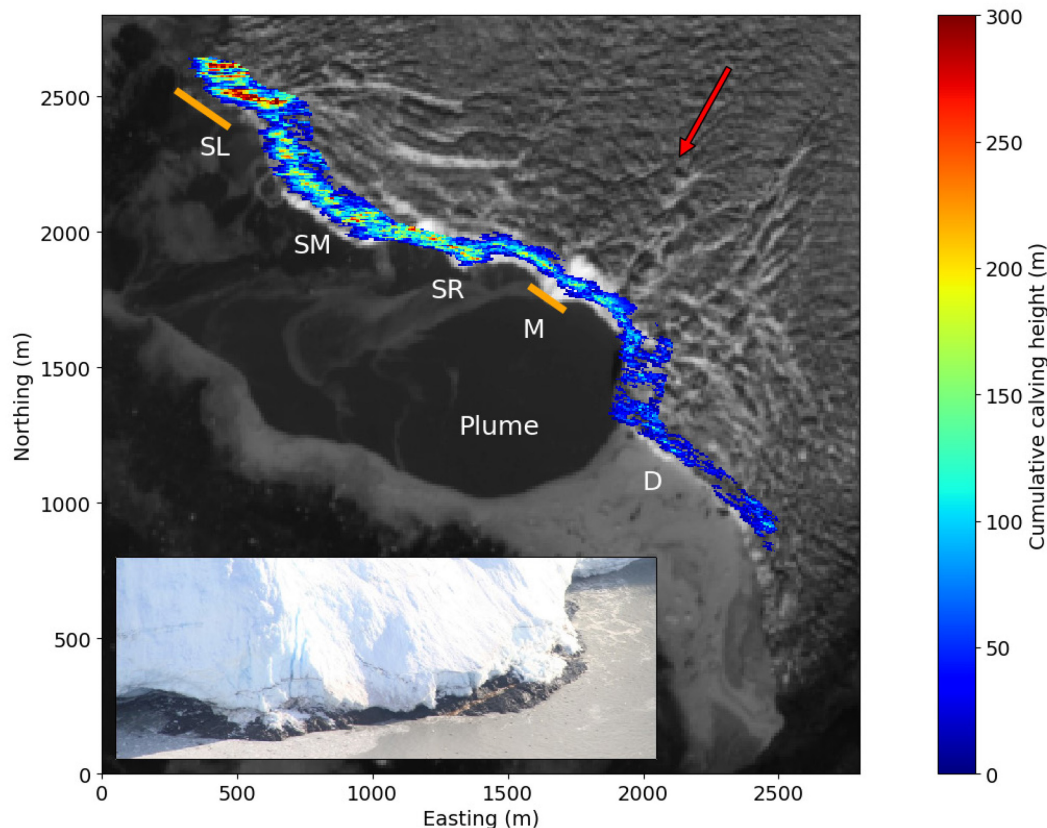


5 deep sector. An overview of the frequencies, volumes and event sizes is given in Table 1. The extracted individual calving event sizes are spread over three orders of magnitude from $0.16 \cdot 10^3 \text{ m}^3$ up to $2.5 \cdot 10^5 \text{ m}^3$. The total volume of all calving events detected in the deep sector is 6.6 times smaller than in the shallow sector. Only small variations in the position of the calving front were observed with the TRI (Fig. S1), which implies that the ice loss by calving is compensated by the ice flow (Fig. 3).

Calving height differences in each radar pixel (ca. 30 m^2 area) were summed up over the measurement period and are referenced to as cumulative calving height. Figure 4 shows that within the shallow sector, the cumulative calving height locally exceeds 300 m, while it is considerably reduced in the deep sector (D). Within the shallow sector variations in cumulative calving height are also observable and thus this sector can be divided into four sub-sectors named SL, SM, SR and M (Figs. 4, 10 5). The highest cumulative calving heights are detected at sector SL, while sector M shows the lowest cumulative heights within the shallow sector. Sector SM has slightly lower values for the cumulative calving height than the sectors SR and SL. For sector D the south-eastern part next to the mainland was not in sight of the radar as it is situated behind a moraine.



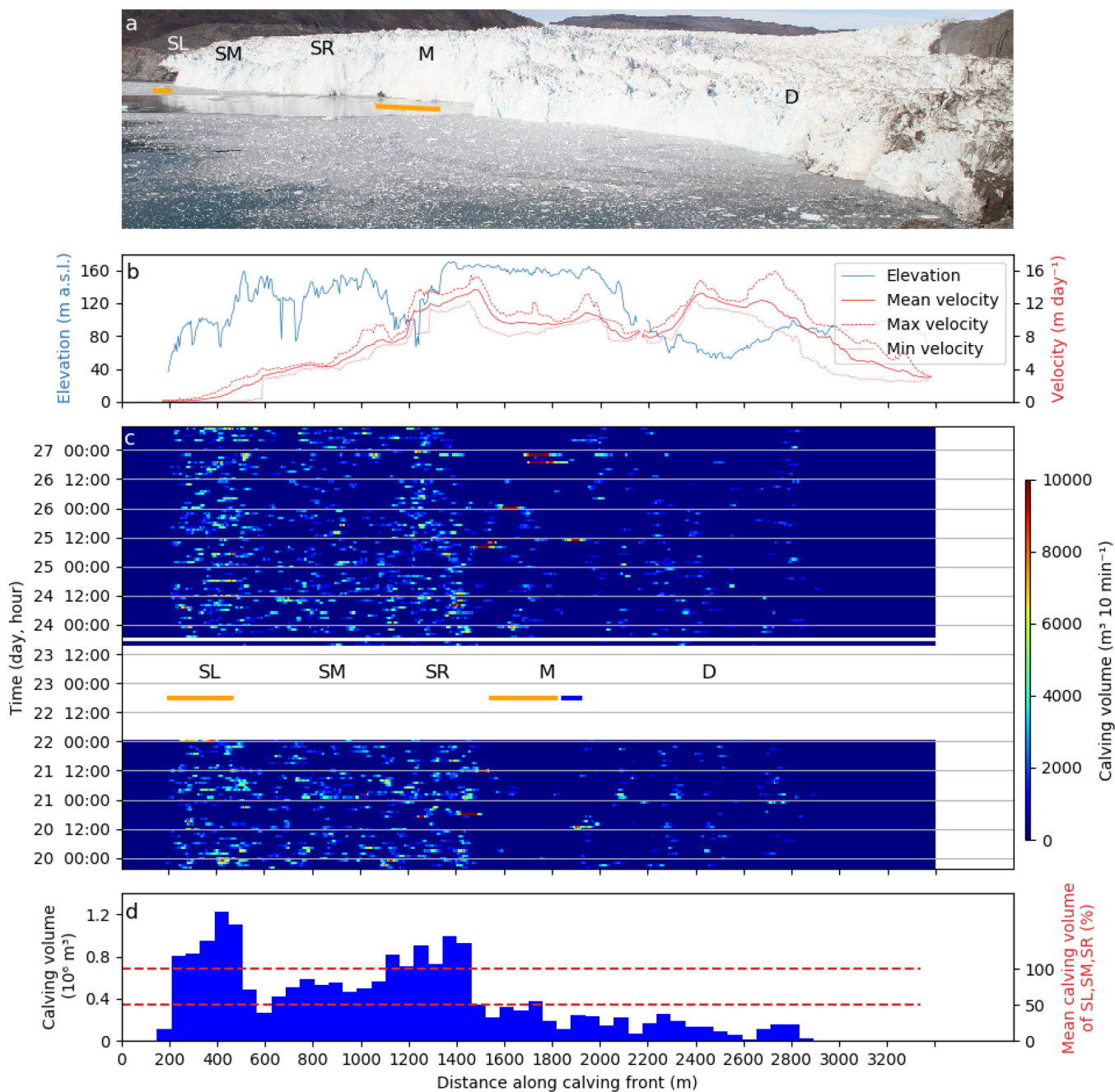
15 **Figure 3: The velocity field at the glacier front. (a) Velocity field measured with the TRI on the 19 August 2016 and (b) with a UAV (between 21 and 25 August 2016; Rohner et al., 2019). The red arrow indicates the general flow direction. The orange line indicates an area where bedrock was observed at the foot of the front. The origin of the coordinate system corresponds to 528350 E / 7741550 N (UTM 22N).**



5 **Figure 4:** Spatial distribution of cumulative calving height in meters over the 6 day measurement period. The capital letters correspond to the different sectors of the calving front (see also Fig. 5a). The deep sector (D) shows lower values than the shallow sector. Variations within the shallow sector were used to define the sectors SL, SM, SR and M. The orange lines indicate areas where bedrock was observed at the foot of the front, which is also shown in the inset. The freshwater plume due to subglacial discharge is well visible.

Table 1: Detected calving events within each sector during the observation period of 6.12 days.

	Whole front	Shallow sector (SL, SM, SR, M)	Deep sector (D)
Total event number	1681	1403	289
Total event volume (m³)	19702000	17129000	2573000
Event sizes			
Mean (m ³)	11700	12200	8900
Median (m ³)	9800	10200	7400
Minimum (m ³)	160	250	160
Maximum (m ³)	248900	248900	101800



5 **Figure 5: The calving front of Eqip Sermia with all calving volume measurements. (a) The calving front with indication of sectors with specific calving behaviour. The different geometry of the sectors SL, SM, SR (steep) and the sector D (flat) are well visible. (b) Elevation and velocity of the cliff top along the glacier front show strong variations. (c) Observed calving volumes in m³ along the front over time. In the data gap the corresponding front sectors are marked. The orange lines indicate bedrock outcrops and the blue line represents the location of the plume. (d) Cumulative calving volume (per bin width of 55 m) in m³ along the front. The right axis shows the percentage of calving volume with respect to the average of sectors SL, SM, SR. 50 % and 100 % are indicated as red dashed lines.**



Figure 5 shows the detailed record of calving activity in the different sectors of the calving front. Figure 5b presents how frontal height and velocity vary. The front height is fluctuating strongly along the front due to the highly crevassed surface. The frontal cliff in the deeper sector D is mostly vertical and between 50 and 80 m high, while in the shallow sector the front is inclined at a slope of 50 degrees and reaching up to 170 m. In general, as already observed in Figure 3, the velocities at the front increase from the margins towards the centre, with the exception of the area around the bedrock outcrop in sector M where velocities are slightly decreased.

Figure 5c summarizes the observed calving activity with event volumes and times. The spatial pattern reflects the pattern shown on the map of cumulative calving height (Fig. 4). In sector D fewer and smaller events were observed than in the sectors SL, SM and SR. The four subsectors of the shallow front show well distinguishable calving event volume patterns throughout the observation period. In the central, very shallow sector M only episodic calving with large volumes was observed. Interestingly, the cumulative calving height in this area is almost a factor 3 smaller as compared to the other shallow sectors and similar to the values observed in the deep sector D. Sector SL with the highest cumulative calving height also has the most individual events, but they are substantially smaller than for sector M.

Figure 5c shows continuous calving activity without any clear temporal pattern throughout the different sectors. The only observable cluster of calving events was detected on 26 August in the afternoon, when a phase with many big events in the sectors M and SR occurred. An important spatial variability of observable calving activity along the front is clearly visible in Figure 5d. The shallow sectors SL and SR contribute the highest volumes, whereas only little calving was observed in the deep sector D.

Given the observations of Figure 5d the important question arises of how much ice mass loss at the calving front remained undetected by the TRI. Assuming constant mass flux over the front, a constant front position, and assuming that the TRI detects all calving volumes in the shallow sectors, less than 25% of the mass loss is detected in sector D.

4.3 Calving statistics

The sizes of the calving events from the different sectors were analysed statistically with the methods described in section 3.1. The event size statistics for the calving events were studied separately for the shallow sectors (SL, SM, SR, M) and the deep sector D and are shown in Figure 6. The distributions of the event sizes differ substantially between the shallow and the deep sector in the number of events (Fig. 6a and b), whereas the shapes of the event size distributions are similar. This results in a much lower cumulative volume of sector D, illustrated by the blue lines in Figures 6a and b. The result of the maximum-likelihood method is shown in Figures 6c and d. The distribution of the deep sector shows a long tail and resembles a power law with an exponent $\alpha = 3.9$ (Fig. 6d). The distribution of the shallow sector follows more closely a log-normal distribution (Fig. 6c) but the log-likelihood ratio R and the probability value p between power law and log-normal is quite small. Therefore, the log-normal model cannot explain the event size distribution of the shallow sector perfectly.

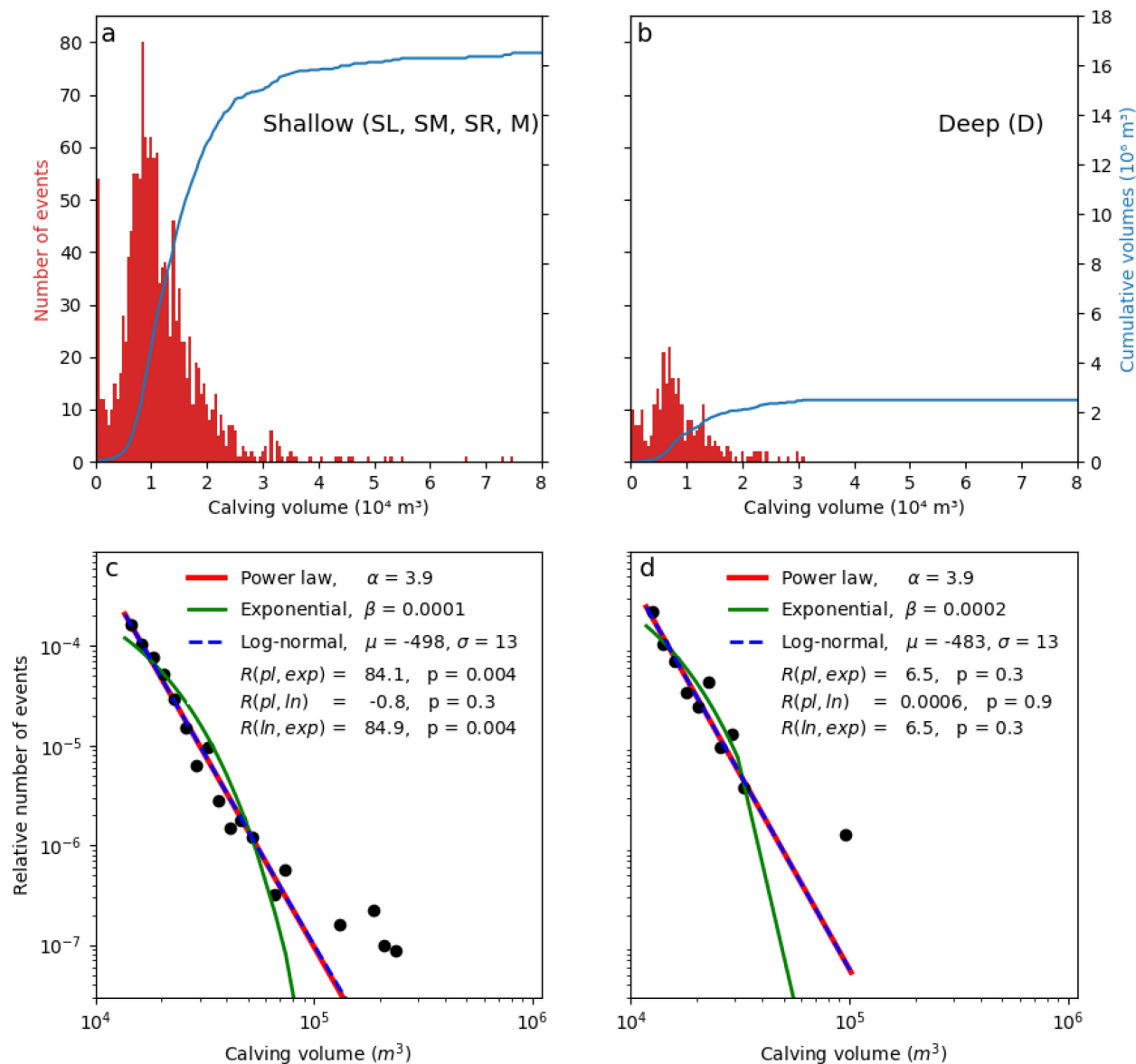


Figure 6: Event size statistics of the observed calving events. (a) The size distribution of the calving events for the shallow sector (b) and the deep sector. (c) Distributions of calving event sizes for the shallow (d) and the deep sectors. Blue, red and green lines represent the best fit power law, exponential and log-normal distribution.

5

4.4 Pressure sensor records

Figure 7 shows the time series of short-term oscillations in the fjord water levels caused by calving events, and recorded by the pressure sensor. The fjord oscillations have a wave amplitude of up to 3.3 m and ranged between several minutes up to about 50 min (Fig. S2). These wave events are in response to single larger calving events with a time delay of 3-4 min. Often



the calving-induced wave events overlay each other and render it difficult to distinguish between subsequent events. Two types of wave oscillations can be observed: The first type has a sharp immediate peak in water height and a slow decrease with time (left inset of Fig. 7). The second type is more symmetric with a gradual increase and decrease of wave amplitude (right inset of Fig. 7).

5

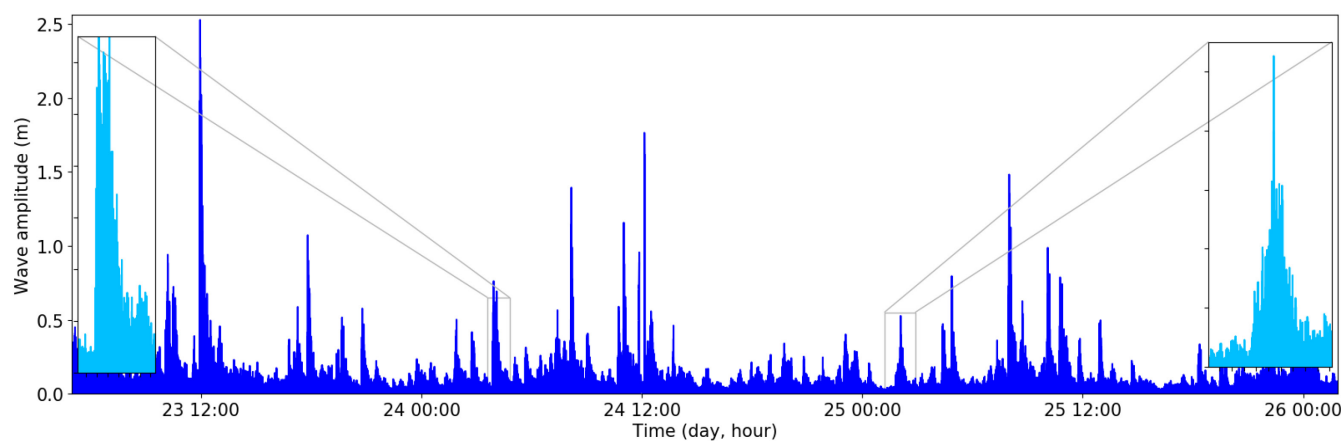


Figure 7: Calving waves detected with a pressure sensor. The light blue panels show details of the two wave types due to calving events. The left one has a sharp immediate peak, while the right one shows gradual increase and decrease of wave amplitude.

10 5 Discussion

Using a terrestrial radar interferometer we were able to produce a detailed and continuous 6.12 day record of calving event volumes along the whole calving front. The detected calving event volumes were highly variable and ranged over three orders of magnitude, consistent with other studies of grounded tidewater glaciers (Chapuis and Tetzlaff, 2014; Pętllicki and Kinnard, 2016; Minowa et al., 2018). The observed calving events show several clusters of events (e.g. on 26 August) but no clear
15 temporal pattern of tidal or diurnal recurrence could be detected.

5.1 Relation to ice flux and other processes

The detected total calving volume agrees with the ice fluxes estimated from the flow speeds and the frontal ice thicknesses (Figs. 3 and 5). Using a mean ice flow velocity of 10 m/day, a front height of 150 m and a front width of 2900 m (the part of the front observable with the TRI) a total ice flux of $4.35 \cdot 10^6 \text{ m}^3$ per day is estimated, which results over the 6.12 day period
20 of observations in a total volume of $26.6 \cdot 10^6 \text{ m}^3$ of ice delivered to the calving front. This value should match up to the observed total calving volume of $19.7 \cdot 10^6 \text{ m}^3$, given the front position is relatively stable (Fig. S1). Total ice flux for the shallow (width 1800 m) and deep sectors (width 1100 m) amounts to $17 \cdot 10^6 \text{ m}^3$ and $10 \cdot 10^6 \text{ m}^3$, respectively. The total calving volume measured with the TRI is for the shallow sector with $17.1 \cdot 10^6 \text{ m}^3$ (Table 1) almost identical, while for the



deep sector the observed calving value is with $2.6 \cdot 10^6 \text{ m}^3$ about 4 times lower than the estimated volume from ice flux. Thus, within the deep sector a large fraction of the ice removed at the terminus is missing from the TRI-calving detection. The filtering of calving events smaller than 160 m^3 and the stacking over 10 min intervals might contribute to this missing volume, but this underestimation of calving volume is also inherent in the shallow sector and therefore is estimated to be rather small.

5 The missing calving volume within the deep sector of $7.4 \cdot 10^6 \text{ m}^3$ can be explained by two main processes. First, this missing volume may be removed by oceanic melt below the water line. The relatively warm saline water provides energy for ice melt where there is contact. Oceanic melt has been shown to be an important process in the mass balance of Greenland's glaciers with estimates of summer melt rates at Eqip Sermia of 0.7 m day^{-1} (Rignot et al., 2010). Assuming an ice thickness of 100 m below the water line for the deep sector this would result in a total oceanic melt volume of $0.47 \cdot 10^6 \text{ m}^3$
10 during the observation period. However, Beaird et al. (2015) showed that this estimate is likely too small as they found a ratio of surface melt derived water to submarine melt of 26% within the fjord, which would result in higher submarine melt rates of 4 m/day when considering the melt water discharge in summer of Rignot et al. (2010). This higher melt rate would result in a total mass loss through oceanic melt of $2.7 \cdot 10^6 \text{ m}^3$, which is however still substantially smaller than the above estimate of the ice flux for the shallow sector. At the shallow sector oceanic melt is less pronounced as the contact area exposed to ocean
15 water is much smaller.

The second process explaining the missing volume is subaqueous calving, which cannot be detected with the TRI. Visual observations by the authors and inspection of high-rate time-lapse camera imagery indicate that subaqueous calving is a frequent process but only occurs at the deep sector of the front.

If these simple estimate for ice flux in the deep and shallow sector holds and the filtered-out volumes from the small events
20 (noise) remain small in comparison, the ocean melt together with the subaqueous calving would provide 75 % of the frontal mass removal from the deep sector.

5.2 Influence from cliff height and shape

The shallow sector of the front with an inclined and higher ice cliff not only shows more but also larger calving events than the deep sector. This can be explained by the different geometries, which have an impact on the calving type as the stress
25 regime is different. Mercenier et al. (2018) showed that an inclined ice cliff results in lower stresses, which can result in larger stable heights of the ice cliff and as a consequence at the shallow sector the calving events can release larger ice volumes. Further, our calving event record suggests that the geometry of the front (cliff height, and slope and water depth) has an important control on the calving type. Calving events in the deep sector mostly occur as whole blocks or towers that fall into the water (visual observation by the authors). In contrast, for the sectors SL, SM, SR and M the calving events can be described
30 mostly as blocks or seracs that are shearing off.

The higher volumes and frequency detected for the sector SL (Fig. 5) can be explained by a rock ridge below the front of this sector. Due to this rock ridge the fjord is very shallow and calving can be detected over almost the full frontal thickness. The strongly episodic but very large calving events in sector M (Fig. 5) might be related to a rock ridge, over which the front is



pushed (Fig. 4). Mercenier et al. (2018) found that for a decreasing water level crevasses tend to open further upstream the glacier, which causes larger calving event sizes.

The foot of the front on the southern side of sector M may be affected by the subglacial meltwater plume surfacing in this area (blue bar in Figs. 4 and 5). Here only a few small events and two larger events on 20 and 25 August can be detected, which also results in low total cumulative calving volumes (Fig. 5d). The formation of a subglacial meltwater channel can lead to undercutting of the calving front due to enhanced submarine melt (Fried et al., 2015), which then may lead to very small events, which are not detectable with the TRI.

5.3 Calving statistics

The size distribution of calving events is best approximated by a power law for the deep front, while for the shallow front a log-normal model seems to better fit the data (Fig. 6c and d). The power law exponent of the deep sector is with $\alpha = 3.9$ rather large compared to other studies, which found an exponent between 1.2 and 2.1 (Chapuis and Tetzlaff, 2014; Åström et al., 2014; Pełlicki and Kinnard, 2016). This could be explained by the missing subaqueous calving events. Observed subaqueous calving events were rather large in volume, which could lead to a lower power law exponent.

As for the deep sector the event size distribution can be represented by a power law model, it is possible that this sector of the front has the characteristics of a self-organized critical system. Those systems are characterised by a slow accumulation of an instability with small, rare events followed by a fast relief of the stresses through events of all magnitudes (Åström et al., 2014). If the deep sector behaves as a self-organized critical system calving event sizes of all magnitudes have to be expected at any time.

For the shallow front the event sizes tend to follow a log-normal distribution, which leads to the suggestion that the acting mechanisms of break-off at this sector of the front are different than for the deep sector. This suggestion seems reasonable as for the shallow front the contact area exposed to sea water is smaller and thus submarine calving less important. A study of Kirkham et al. (2017) supports those findings as they suggests by looking at size distribution of icebergs that a reduction of the number of mechanisms in their disintegration and thus a simplifying complexity leads to the transition from power law to log-normal distributions.

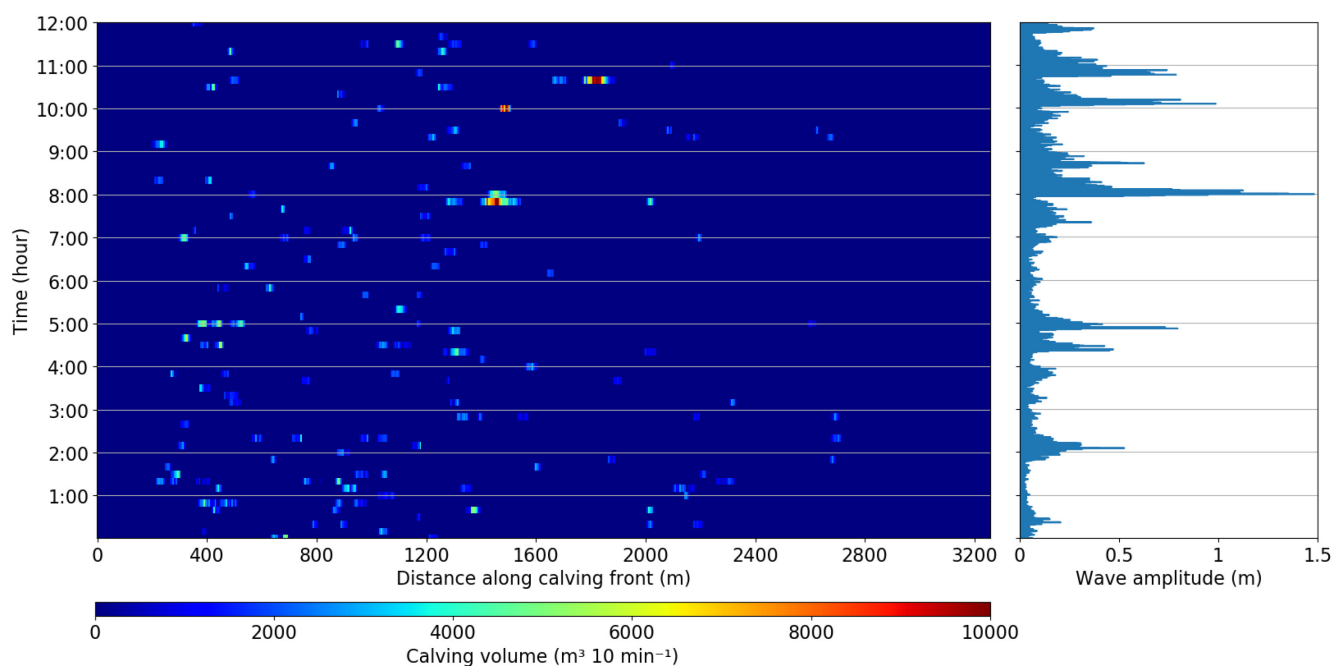
25 5.4 Comparison with pressure sensor data

Figure 8 shows a comparison of pressure sensor data and detected calving events during a 12 hour period. Bigger events are clearly visible in both data sets. Those events look mostly like the first asymmetric type described in section 4.4 and displayed in Figure 7. The second symmetric type can be found in the pressure sensor data, but mostly they cannot be clearly assigned to a single event in the TRI dataset. These events, like the one at 2:00 (Fig. 8), likely are due to larger subaqueous calving events in the deep sector (Sect. 5.1) with big up-floating icebergs that cannot be detected by the TRI. These subaquatic calving events could explain parts of the missing calving volume. This reasoning is supported by other studies who found that subaerial events have a gradually decreasing amplitude after the maximum wave amplitude, while subaqueous calving events showed



no clear onset and a sudden drop of the amplitude after the maximum wave amplitude (Minowa et al., 2018). For verification of this distinction between subaquatic and subaerial calving events additional observations, such as time-lapse cameras with a high temporal resolution, would be required.

In summary, the pressure sensor data together with the calving volume record (Fig. 8) indicate that large events can be well detected from pressure sensor data. Thus, potentially pressure sensor observation could be exploited as a simple method to derive calving event numbers, volumes and potentially even style (subaerial or subaqueous).



10 **Figure 8: Comparison between pressure sensor derived wave amplitudes (right) and detected calving events (left) for a 12 hour period on 25 August. Big calving events are clearly visible in both data sets.**

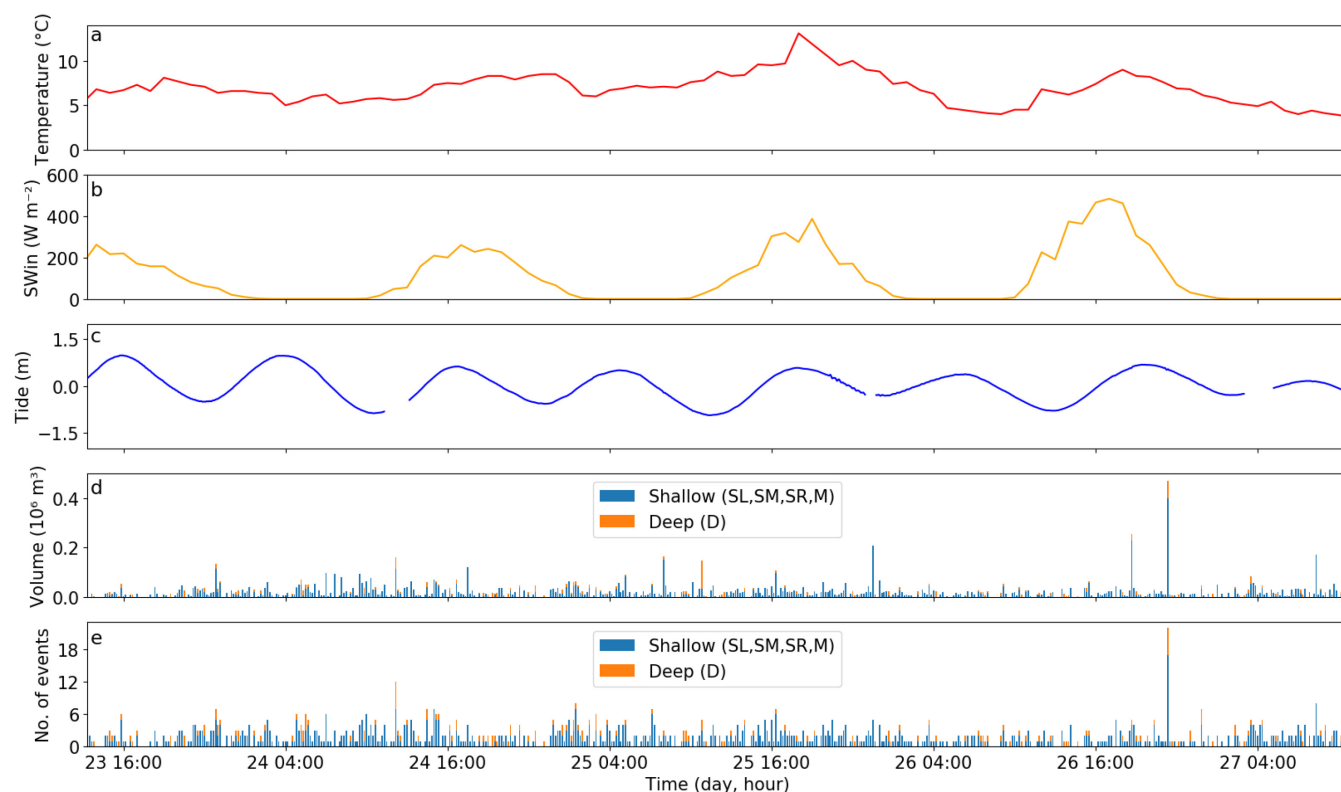
5.5 Relation to external forcings

Calving activity has been hypothesized to be triggered by external forcings such as melt water accumulation in crevasses (Benn et al., 2007) and changes in stress state due to tides (Bartholomaeus et al., 2015). Therefore, calving activity should be linked to high air temperatures and incoming radiation leading to surface melt.

Figure 9 compares air temperature, incoming shortwave radiation and tides with volume and number of calving events for the second part of the observation period (the first part is shown in Fig. S3). This comparison does not show any clear relationship. As the observation time of 6 days is rather short even if no significant correlations between detected events and environmental forcings are obtained, it does not exclude an influence on the calving activity. Consistent with our observations, Pełlicki and Kinnard (2016) and Chapuis and Tetzlaff (2014) also found that the calving activity during their observation period of a few



days was not dependent on environmental forcings, while others found an influence of ocean temperature on calving activity over seasonal timescales (Luckman et al., 2015; Schild et al., 2018).



5 **Figure 9: Comparison of forcing to detected calving. (a) Air temperature from the AWS1 for the second part of the observation period. (b) Incoming shortwave radiation. (c) Tidal range in meters. (d) Volume of calving events in m^3 for the shallow and deep sectors. (e) Number of calving events.**

6 Conclusion

10 We developed a novel method to establish a detailed, spatially resolved calving event catalogue and statistics and to quantify calving volumes and source areas. During 6 days 1681 calving events were identified for the whole calving front of which 85% in the shallow sector. Calving events of the shallow sector have a larger mean volume of $12200 m^3$ as compared to $8900 m^3$ for the deep sector. Assuming similar ice flux in both sectors the missing calving volume of the deep sector has to be explained by other processes than aerial calving. Our analysis shows that in the deep sector the mass loss due to subaqueous calving and oceanic melt likely contributes 75 % to the total mass loss. The event size distributions of the two sectors follow a power law and a log-normal model, respectively. The variations of the calving event sizes and number of events for the different sectors can be explained by the bed topography and the calving front geometry. The shallow sector is characterised

15



by an inclined front and shows a different calving type than the deep sector and calving events can release larger ice volumes. A rock ridge in the center of the calving front influences the calving activity and leads to fewer but larger events.

Comparing the detected calving events with pressure sensor data shows that the big events are clearly discernible in both data sets. Some events in the pressure sensor data, which are not visible in the TRI data, show a different shape in the wave
5 oscillation and likely correspond to subaqueous calving events. For the short time span of the observations no relationship between the observed calving activity and environmental forcings (tides, temperature, incoming shortwave radiation) could be established.

This study shows the potential of detailed high-rate observations to elucidate the processes and forcings leading to iceberg calving from tidewater glaciers. The resulting statistics of calving event sizes in relation to geometry, bathymetry and external
10 forcings are important benchmarks for calving models. Testing and calibrating such models with field data is mandatory for the understanding of the delicate dynamics of outlet glaciers which control the dynamics of large parts of the Greenland ice sheet.

Code and data availability. Data and codes are available from the authors upon request.

15 *Competing interests.* The authors declare that they have no conflict of interest.

Acknowledgments. We thank Diego Wasser and Rémy Mercenier for help during the field campaign at Eqip Sermia. This work was funded by University of Zurich and ETH Zurich, Switzerland. The field work was supported through grants 200021-156098 and 200021-153179/1 of the Swiss National Science Foundation.

20 *Author contributions.* A. Walter, M. P. Lüthi and A. Vieli designed the manuscript. A. Walter performed all analysis and wrote the draft of the manuscript. All authors contributed to the final version of the manuscript.

References

Alstott, J., Bullmore, E., and Plenz, D.: powerlaw. A Python package for analysis of heavy-tailed distributions, PloS ONE 9 (1): e85777, <https://doi.org/10.1371/journal.pone.0085777>, 2014.

25 Amundson, J. M., Clinton, J. F., Fahnestock, M., Truffer, M., Lüthi, M. P., and Motyka, R. J.: Observing calving-generated ocean waves with coastal broadband seismometers, Jakobshavn Isbræ, Greenland, Ann. Glaciol. 53 (60), 79–84, <https://doi.org/10.3189/2012/AoG60A200>, 2012.

Åström, J. A., Vallot, D., Schäfer, M., Welty, E. Z., O’Neel, S., Bartholomäus, T. C., Liu, Yan, Riikilä, T. I., Zwinger, T., Timonen, J., and Moore, J. C.: Termini of calving glaciers as self-organized critical systems, Nature Geoscience 7 (12), 874–878, <https://doi.org/10.1038/NGEO2290>, 2014.



- Bartholomaus, T. C., Larsen, Ch. F., O'Neel, S., and West, M. E.: Calving seismicity from iceberg-sea surface interactions, *J. Geophys. Res.* 117 (F4), <https://doi.org/10.1029/2012JF002513>, 2012.
- Bartholomaus, T. C., Larsen, Ch. F., West, M. E., O'Neel, S., Pettit, E. C., and Truffer, M.: Tidal and seasonal variations in calving flux observed with passive seismology, *J. Geophys. Res. Earth Surf.* 120 (11), 2318–2337,
5 <https://doi.org/10.1002/2015JF003641>, 2015.
- Beaird, N., Straneo, F., and Jenkins, W.: Spreading of Greenland meltwaters in the ocean revealed by noble gases, *Geophys. Res. Lett.* 42 (18), 7705–7713, <https://doi.org/10.1002/2015GL065003>, 2015.
- Benn, D. I., Warren, Ch. R., and Mottram, R. H.: Calving processes and the dynamics of calving glaciers, *Earth-Science Reviews* 82 (3-4), 143–179, <https://doi.org/10.1016/j.earscirev.2007.02.002>, 2007.
- 10 Caduff, R., Schlunegger, F., Kos, A., and Wiesmann, A.: A review of terrestrial radar interferometry for measuring surface change in the geosciences, *Earth Surf. Process. Landforms* 40 (2), 208–228, <https://doi.org/10.1002/esp.3656>, 2015.
- Carr, R. J., Bell, H., Killick, R., and Holt, T.: Exceptional retreat of Novaya Zemlya's marine-terminating outlet glaciers between 2000 and 2013, *The Cryosphere* 11 (5), 2149–2174, <https://doi.org/10.5194/tc-11-2149-2017>, 2017.
- Cassotto, R., Fahnestock, M., Amundson, J. M., Truffer, M., Boettcher, M. S., de la Pena, S., and Howat, I.: Non-linear glacier
15 response to calving events, Jakobshavn Isbræ, Greenland, *J. Glaciol.* 4, 1–16, <https://doi.org/10.1017/jog.2018.90>, 2018.
- Catania, G. A., Stearns, L. A., Sutherland, D. A., Fried, M. J., Bartholomaus, T. C., Morlighem, M., Shroyer, E., and Nash, J.: Geometric Controls on Tidewater Glacier Retreat in Central Western Greenland, *Journal of Geophysical Research: Earth Surface*, 123, 2024–2038, <https://doi.org/10.1029/2017JF004499>, 2018.
- Chapuis, A., Rolstad, C., and Norland, R.: Interpretation of amplitude data from a ground-based radar in combination with
20 terrestrial photogrammetry and visual observations for calving monitoring of Kronebreen, Svalbard, *Ann. Glaciol.* 51 (55), 34–40, <https://doi.org/10.3189/172756410791392781>, 2010.
- Chapuis, A., and Tetzlaff, T.: The variability of tidewater-glacier calving. Origin of event-size and interval distributions, *J. Glaciol.* 60 (222), 622–634, <https://doi.org/10.3189/2014JoG13J215>, 2014.
- Clauset, A., Shalizi, C. R., and Newman, M. E. J.: Power-Law Distributions in Empirical Data, *SIAM Rev.* 51 (4), 661–703,
25 <https://doi.org/10.1137/070710111>, 2009.



- Enderlin, E. M., Howat, I. M., Jeong, S., Noh, M.-J., van Angelen, J. H., and van den Broeke, M. R.: An improved mass budget for the Greenland ice sheet, *Geophys. Res. Lett.* 41 (3), 866–872, <https://doi.org/10.1002/2013GL059010>, 2014.
- Fried, M. J., Catania, G. A., Bartholomaeus, T. C., Duncan, D., Davis, M., Stearns, L. A., Nash, J., Shroyer, E., and Sutherland, D.: Distributed subglacial discharge drives significant submarine melt at a Greenland tidewater glacier, *Geophys. Res. Lett.* 5 42 (21), 9328–9336, <https://doi.org/10.1002/2015GL065806>, 2015.
- Glowacki, O., Deane, G. B., Moskalik, M., Blondel, Ph., Tegowski, J., and Blaszczyk, M.: Underwater acoustic signatures of glacier calving, *Geophys. Res. Lett.* 42 (3), 804–812, <https://doi.org/10.1002/2014GL062859>, 2015.
- Goldstein, R.: Atmospheric limitations to repeat-track radar interferometry, *Geophys. Res. Lett.* 22 (18), 2517–2520, <https://doi.org/10.1029/95GL02475>, 1995.
- 10 Holland, D. M., Thomas, R. H., de Young, B., Ribergaard, M. H., and Lyberth, B.: Acceleration of Jakobshavn Isbræ triggered by warm subsurface ocean waters, *Nature Geosci* 1 (10), 659–664, <https://doi.org/10.1038/ngeo316>, 2008.
- Howat, I. M., Box, J. E., Ahn, Y., Herrington, A., and McFadden, E. M.: Seasonal variability in the dynamics of marine-terminating outlet glaciers in Greenland, *J. Glaciol.* 56 (198), 601–613, <https://doi.org/10.3189/002214310793146232>, 2010.
- IPCC 2013 (Hg.): Climate change 2013. The physical science basis: Working Group I contribution to the Fifth assessment report of the Intergovernmental Panel on Climate Change. Cambridge: Cambridge University Press, <https://doi.org/10.1017/CBO9781107415324>, 2014.
- 15 Joughin, I., Abdalati, W., and Fahnestock, M.: Large fluctuations in speed on Greenland's Jakobshavn Isbrae glacier, *Nature* 432 (7017), 608–610, <https://doi.org/10.1038/nature03130>, 2004.
- Jouvet, G., Weidmann, Y., Seguinot, J., Funk, M., Abe, T., Sakakibara, D., Seddik, H., and Sugiyama, S.: Initiation of a major calving event on the Bowdoin Glacier captured by UAV photogrammetry, *The Cryosphere* 11 (2), 911–921, <https://doi.org/10.5194/tc-11-911-2017>, 2017.
- 20 King, M. D., Howat, I. M., Jeong, S., Noh, M. J., Wouters, B., Noël, B., and van den Broeke, M. R.: Seasonal to decadal variability in ice discharge from the Greenland Ice Sheet, *The Cryosphere* 12 (12), 3813–3825, <https://doi.org/10.5194/tc-12-3813-2018>, 2018.
- Kirkham, J. D., Rosser, N. J., Wainwright, J., Vann Jones, E. C., Dunning, St. A., Lane, V. S., Hawthorn, D. E., Strzelecki, M. C., and Szczuciński, W.: Drift-dependent changes in iceberg size-frequency distributions, *Scientific reports* 7 (1), 15991, <https://doi.org/10.1038/s41598-017-14863-2>, 2017.



- Luckman, A., Benn, D. I., Cottier, F., Bevan, S., Nilsen, F., and Inall, M.: Calving rates at tidewater glaciers vary strongly with ocean temperature, *Nature communications* 6, 8566, <https://doi.org/10.1038/ncomms9566>, 2015.
- Lüthi, M. P., and Vieli, A.: Multi-method observation and analysis of a tsunami caused by glacier calving, *The Cryosphere* 10 (3), 995–1002, <https://doi.org/10.5194/tc-10-995-2016>, 2016.
- 5 Lüthi, M. P., Vieli, A., Moreau, L., Joughin, I., Reisser, M., Small, D., and Stober, M.: A century of geometry and velocity evolution at Eqip Sermia, West Greenland, *J. Glaciol.* 62 (234), 640–654, <https://doi.org/10.1017/jog.2016.38>, 2016.
- McFadden, E. M., Howat, I. M., Joughin, I., Smith, B. E., and Ahn, Y.: Changes in the dynamics of marine terminating outlet glaciers in west Greenland (2000–2009), *J. Geophys. Res.* 116, F02022, <https://doi.org/10.1029/2010JF001757>, 2011.
- Mercenier, R., Lüthi, M. P., and Vieli, A.: Calving relation for tidewater glaciers based on detailed stress field analysis, *The*
10 *Cryosphere* 12 (2), 721–739, <https://doi.org/10.5194/tc-12-721-2018>, 2018.
- Minowa, M., Podolskiy, E. A., Sugiyama, S., Sakakibara, D., and Skvarca, P.: Glacier calving observed with time-lapse imagery and tsunami waves at Glaciar Perito Moreno, Patagonia, *J. Glaciol.* 64 (245), 62–376, <https://doi.org/10.1017/jog.2018.28>, 2018.
- Moon, T., Joughin, I., Smith, B., and Howat, I.: 21st-century evolution of Greenland outlet glacier velocities, *Science* (New
15 York, N.Y.) 336 (6081), 576–578, <https://doi.org/10.1126/science.1219985>, 2012.
- Nick, F. M., Vieli, A., Howat, I. M., and Joughin, I.: Large-scale changes in Greenland outlet glacier dynamics triggered at the terminus, *Nature Geosci* 2 (2), 110–114, <https://doi.org/10.1038/ngeo394>, 2009.
- O’Neel, S., Echelmeyer, K. A., and Motyka, R. J.: Short-term variations in calving of a tidewater glacier. LeConte Glacier, Alaska, U.S.A, *J. Glaciol.* 49 (167), 587–598, <https://doi.org/10.3189/172756503781830430>, 2003.
- 20 O’Neel, S., Larsen, Ch. F., Rupert, N., and Hansen, R.: Iceberg calving as a primary source of regional-scale glacier-generated seismicity in the St. Elias Mountains, Alaska, *J. Geophys. Res.* 115, L22501, <https://doi.org/10.1029/2009JF001598>, 2010.
- Pełlicki, M., and Kinnard, Ch.: Calving of Fuerza Aérea Glacier (Greenwich Island, Antarctica) observed with terrestrial laser scanning and continuous video monitoring, *J. Glaciol.* 62 (235), 835–846, <https://doi.org/10.1017/jog.2016.72>, 2016.
- Porter, C., Morin, P., Howat, I., Noh, M.-J., Bates, B., Peterman, K., Keeseey, S., Schlenk, M., Gardiner, J., Tomko, K., Willis,
25 M., Kelleher, C., Cloutier, M., Husby, E., Foga, S., Nakamura, H., Platson, M., Wethington, M., Jr., Williamson, C., Bauer,



- G., Enos, J., Arnold, G., Kramer, W., Becker, P., Doshi, A., D'Souza, C., Cummins, P., Laurier, F., and Bojesen, M.: "ArcticDEM", Harvard Dataverse, V1, <https://doi.org/10.7910/DVN/OHHUKH>, 2018.
- Pralong, A., and Funk, M.: Dynamic damage model of crevasse opening and application to glacier calving, *J. Geophys. Res.* 110, B01309, <https://doi.org/10.1029/2004JB003104>, 2005.
- 5 Rignot, E., Velicogna, I., van den Broeke, M. R., Monaghan, A., and Lenaerts, J. T. M.: Acceleration of the contribution of the Greenland and Antarctic ice sheets to sea level rise, *Geophys. Res. Lett.* 38 (5), <https://doi.org/10.1029/2011GL046583>, 2011.
- Rignot, E., Fenty, I., Xu, Y., Cai, C., and Kemp, Ch.: Undercutting of marine-terminating glaciers in West Greenland, *Geophys. Res. Lett.* 42 (14), 5909–5917, <https://doi.org/10.1002/2015GL064236>, 2015.
- 10 Rignot, E., Koppes, M., and Velicogna, I.: Rapid submarine melting of the calving faces of West Greenland glaciers, *Nature Geosci* 3 (3), 187–191, <https://doi.org/10.1038/ngeo765>, 2010.
- Rohner, Ch., Small, D., Henke, D., Lüthi, M. P., and Vieli, A.: Multisensor validation of tidewater glacier flow fields derived from SAR intensity tracking, *The Cryosphere Discuss.*, 1–27, <https://doi.org/10.5194/tc-2018-278>, 2019.
- Rolstad, C., and Norland, R.: Ground-based interferometric radar for velocity and calving-rate measurements of the tidewater glacier at Kronebreen, Svalbard, *Ann. Glaciol.* 50 (50), 47–54, <https://doi.org/10.3189/172756409787769771>, 2009.
- Schild, K. M., Renshaw, C. E., Benn, D. I., Luckman, A., Hawley, R. L., How, P., Trusel, L., Cottier, F. R., Pramanik, A., and Hulton, N. R. J.: Glacier Calving Rates Due to Subglacial Discharge, Fjord Circulation, and Free Convection, *J. Geophys. Res. Earth Surf.* 123 (9), 2189–2204, <https://doi.org/10.1029/2017JF004520>, 2018.
- Straneo, F., Heimbach, P., Sergienko, O., Hamilton, G., Catania, G. A., Griffies, S., Hallberg, R., Jenkins, A., Joughin, I., 20 Motyka, R., Pfeffer, T. W., Price, S. F., Rignot, E., Scambos, T., Truffer, M., and Vieli, A.: Challenges to Understanding the Dynamic Response of Greenland's Marine Terminating Glaciers to Oceanic and Atmospheric Forcing, *Bull. Amer. Meteor. Soc.* 94 (8), 1131–1144, <https://doi.org/10.1175/BAMS-D-12-00100.1>, 2013.
- Strozzi, T., Werner, Ch., Wiesmann, A., and Wegmüller, U.: Topography Mapping With a Portable Real-Aperture Radar Interferometer, *IEEE Geoscience And Remote Sensing Letters* 9 (2), 277–281, <https://doi.org/10.1109/LGRS.2011.2166751>, 25 2012.
- Thomas, R. H.: Force-perturbation analysis of recent thinning and acceleration of Jakobshavn Isbræ, Greenland, *J. Glaciol.* 50 (168), 57–66, <https://doi.org/10.3189/172756504781830321>, 2004.



- Vallot, D., Adinugroho, S., Strand, R., How, P., Pettersson, R., Benn, D. I., and Hulton, N. R. J.: Automatic detection of calving events from time-lapse imagery at Tunabreen, Svalbard, *Geosci. Instrum. Method. Data Syst.* 8 (1), 113–127, <https://doi.org/10.5194/gi-8-113-2019>, 2019.
- van der Walt, S., Schönberger, J. L., Nunez-Iglesias, J., Boulogne, F., Warner, J. D., Yager, N., Gouillart, E., and Yu, T.: scikit-image. Image processing in Python, *PeerJ* 2, e453, <https://doi.org/10.7717/peerj.453>, 2014.
- Vieli, A., and Nick, F. M.: Understanding and Modelling Rapid Dynamic Changes of Tidewater Outlet Glaciers. *Issues and Implications*, *Surv Geophys* 32 (4-5), 437–458, <https://doi.org/10.1007/s10712-011-9132-4>, 2011.
- Voytenko, D., Stern, A., Holland, D. M., Dixon, T. H., Christianson, K., and Walker, R. T.: Tidally driven ice speed variation at Helheim Glacier, Greenland, observed with terrestrial radar interferometry, *J. Glaciol.* 61 (226), 301–308, <https://doi.org/10.3189/2015JoG14J173>, 2015.
- Walter, F., Olivieri, M., and Clinton, J. F.: Calving event detection by observation of seiche effects on the Greenland fjords, *J. Glaciol.* 59 (213), 162–178, <https://doi.org/10.3189/2013JoG12J118>, 2013.
- Walter, F., O'Neel, S., McNamara, D., Pfeffer, W. T., Bassis, J. N., and Fricker, H. A.: Iceberg calving during transition from grounded to floating ice. *Columbia Glacier, Alaska*, *Geophys. Res. Lett.* 37 (15), <https://doi.org/10.1029/2010GL043201>, 2010.
- Warren, Ch. R.: Terminal environment, topographic control and fluctuations of West Greenland glaciers, *Boreas* 20 (1), 1–15, <https://doi.org/10.1111/j.1502-3885.1991.tb00453.x>, 1991.
- Warren, Ch. R., Glasser, N. F., Harrison, S., Winchester, V., Kerr, A. R., and Rivera, A.: Characteristics of tide-water calving at Glaciär San Rafael, Chile, *J. Glaciol.* 41 (138), 273–289, <https://doi.org/10.3189/S0022143000016178>, 1995.
- Werner, Ch., Strozzi, T., Wiesmann, A., and Wegmüller, U.: A Real-Aperture Radar for Ground-Based Differential Interferometry, *IGARSS Conference Paper*, 210-213, <https://doi.org/10.1109/IGARSS.2008.4779320>, 2008a.
- Werner, Ch., Strozzi, T., Wiesmann, A., and Wegmüller, U.: Gamma's portable radar interferometer, *Symposium on Deformation Measurement and Analysis*, 2008b.
- Xie, S., Dixon, T. H., Voytenko, D., Deng, F., and Holland, D. M.: Grounding line migration through the calving season of Jakobshavn Isbræ, Greenland, observed with terrestrial radar interferometry, *The Cryosphere Discuss.*, 1–29, <https://doi.org/10.5194/tc-2017-231>, 2018.